

# A radiation transport coupled particle-in-cell simulation. II. Simulation results in a one-dimensional planar model

Hae June Lee<sup>a)</sup> and J. P. Verboncoeur

*Department of Electrical Engineering and Computer Science, University of California, Berkeley, California 94720-1770*

(Received 14 December 2000; accepted 30 March 2001)

The radiation-transport coupled particle-in-cell model is applied to one-dimensional planar model to investigate the radiation trapping phenomena in relatively high- and low-pressure Ar glow discharges. The radiation intensity spectra and the total radiation flux are calculated from the radiative excited-state profile. The simulation results for Doppler and resonance collision broadenings are compared with the eigenmode description of the Holstein equation, with good agreement. Observed are the effects of radiation trapping of photons, diffusion, collisional quenching, and step ionization from excited states on the discharge properties. © 2001 American Institute of Physics. [DOI: 10.1063/1.1373679]

## I. INTRODUCTION

Resonance radiation is an important energy transport mechanism in lamp discharges, in which radiation efficiency ranges from 50% to 75%.<sup>1</sup> In addition, radiation transport is an important factor to improve the performances of plasma devices for lighting such as fluorescent lamps, plasma display panels, and dielectric barrier discharges. Therefore, it is necessary to develop a full plasma simulation including radiation transport and various collisions among species in order to understand the basic physics and to improve the efficiency and photometric properties of such systems.

Many researchers developed radiation transport models, and the history and the methods of the models are described in the preceding Part I. The simplest method to include radiation trapping effect is to use the effective decay rate with the trapping factor of the lowest mode of the solutions of the Holstein–Biberman equation<sup>2–4</sup> instead of the vacuum decay rate.<sup>5</sup> This method is adequate if the spatial distribution of the radiative excited-state density is close to the lowest mode solution of the Holstein–Biberman equation, but cannot represent the redistribution of the excited-state density by the radiation trapping effect. Another method is to treat the problem with the Monte Carlo (MC) photon simulation,<sup>6,7</sup> which is useful for arbitrary line shapes, partial frequency redistribution (PFR), and any complex geometry. The MC method, however, has disadvantages in self-consistent time-dependent radiation transport simulation with plasma motions due to its expensive computation cost. Instead of the MC method, Lawler *et al.* developed a numerical method called the propagator function method (PFM),<sup>8</sup> which solves the Holstein–Biberman equation in a way similar to fluid models by adding the radiation transport term with a kernel function called a propagator. This method is faster than the MC method and capable of calculating the time-dependent evolution of the radiative state self-consistently.

In this study, the fluid description of the Holstein–

Biberman equation is coupled with the particle-in-cell code for planar geometry, XPDP1,<sup>9</sup> using a PFM which is similar to that of Lawler *et al.*<sup>8</sup> The PFM of this model is modified to be able to include arbitrary line shapes and applicable to any nonuniform distribution of the ground-state density.

The aim of this study is to verify the RT-PIC model and to investigate the role of radiation transport in glow discharges rather than to simulate a realistic fluorescent lamp discharge; therefore, we simulate an Ar discharge due to the well-known discharge properties of Ar, even though it is not a proper reaction gas for lamp discharges or lighting devices.

We simulate relatively high- and low-pressure Ar direct current (dc) discharges where the Lorentz and the Doppler line shapes are dominant, respectively. The line shape of emitted photons is broadened by the influences of the physical condition of the ground-state atoms or any other disturbing atoms. Two important line broadenings are Doppler and pressure broadenings.<sup>10</sup> Doppler broadening is caused by the Doppler shift of light due to the thermal motion of the photon-emitting atoms; the temperature of the ground-state atoms affects the linewidth. Pressure broadening is influenced by collisions with disturbing atoms. Therefore, the densities of the same species or other species affect the linewidth. We classify the pressure broadening as foreign gas broadening if the disturbing atoms are different species from the photon-emitting atom, and resonance collision broadening if the disturbing atoms are the same species. Both have the dispersive line shape of a Lorentzian distribution, called the Lorentz line shape. Doppler broadening has a Gaussian distribution of line shape over frequency which is called the Doppler line shape. The Doppler broadening is dominant at a low-pressure regime and the pressure broadening is dominant at a high-pressure regime. In the intermediate pressure regime, however, both pressure and Doppler broadenings are important. Thus, we should use the Voigt line shape which includes the effects of both. In this regime, the assumption of complete frequency redistribution (CFR) is not valid because of the mixed broadening mechanism. Payne *et al.*<sup>11</sup> and

<sup>a)</sup>Electronic mail: leehj@eecs.berkeley.edu

TABLE I. Simulation input parameters and other related physical quantities.

	Case 1	Case 2
System length, $L$ (cm)	1	1
Gas pressure, $p$ (Torr)	0.01	1.0
Applied energy source	a	b
Debye length, $\lambda_{De}$ (cm)	0.04	0.0037
Time step for PIC-MCC, $\Delta t$ (ns)	0.025	0.01
Time step for RT, $\Delta t_r/\tau_v$	0.051	0.0051
Cell size for PIC-MCC (cm)	0.01	0.002
Cell size for RT, $\Delta z$ (cm)	0.01	0.01
Initial condition	c	d
Dominant broadening	Doppler	Pressure
Linewidth, $\Delta\nu$ (GHz)	5.59	1.208
Opacity, $k_0L$	$3.62 \times 10^2$	$1.13 \times 10^6$
Trapping factor, $g_0$	757.1	$1.65 \times 10^3$
Transmission <sup>e</sup> for a cell	0.14	0.0053
Diffusion coefficient ( $\text{m}^2/\text{s}$ )	1.396	0.014

<sup>a</sup>dc 25 V and weak electron beam injection ( $0.1 \text{ mA}/\text{cm}^2$ ) which induces a temperature-limited-mode discharge (Ref. 14).

<sup>b</sup>dc 120 V and secondary electron emission by ion impact on the cathode at  $z=0.01 \text{ m}$ , with a secondary electron emission coefficient  $\gamma_{se}=0.2$ .

<sup>c</sup>Zero plasma density  $n_e=n_i=0$ , and zero excited-state densities  $n^m=n^r=0$ .

<sup>d</sup>Uniform plasma density  $n_e=n_i=10^{17} \text{ m}^{-3}$  and zero excited-state densities  $n^m=n^r=0$ .

<sup>e</sup>Transmission factor for a cell size  $\Delta z$  in uniform ground-state density  $T(k_0\Delta z)$ .

Post<sup>12</sup> showed the discrepancy by comparing effective decay times from experiments with the theory results with the CFR assumption for Ar and Hg, respectively. We assume CFR in this model and do not consider the Voigt line shape. A future study will include the Voigt line shape with the PFR assumption for the intermediate pressure regime.

We describe the input parameters and the simulation conditions of the low- and the high-pressure cases in Sec. II. The results of each case for uniform and nonuniform ground-state densities are presented in Sec. III. Radiation fluxes and spectra for both cases are discussed there too. In Sec. IV, we compare the simulation result of the radiative excited-state profile with Holstein's eigenmode solutions for the Doppler and the Lorentz line shapes. Finally, a summary and discussions are presented in Sec. V.

## II. SIMULATION CONDITIONS

As described in Part I, we consider only two energy levels of the first excited states of Ar ( $3s^23p^54s$ ), one metastable ( $^3P_2$ ) and one radiative state ( $^1P_1$ ), which has a vacuum radiative decay time  $\tau_v=1.96 \text{ ns}$  with a wavelength  $\lambda_0=104.82 \text{ nm}$ . We simulate dc discharges with pressures of 1 Torr and 10 mTorr where pressure and Doppler broadenings are dominant, respectively. The simulation parameters and basic quantities of radiation properties for each case are listed in Table I. Because we consider only Ar species, the Lorentz line shape comes from resonance collision broadening where the linewidth is proportional to the absorbing ground-state density. Uniform gas density and constant gas temperature of 300 K is assumed, and the trapping factors are calculated for a 1 cm planar gap with the approximation equations from Molisch *et al.*<sup>13</sup>

TABLE II. Collision processes of neutral atoms (from Table I of Ref. 16).

Reaction	Symbol	Rate coefficient ( $\text{m}^{-3}/\text{s}$ )
$\text{Ar}^m + e \rightarrow \text{Ar}^r + e$	$K_r$	$2 \times 10^{-13}$
$\text{Ar} + \text{Ar}^* \rightarrow \text{Ar} + \text{Ar}$	$K_{cq}$	$3 \times 10^{-21}$
$\text{Ar}^* + \text{Ar}^* \rightarrow \text{Ar} + \text{Ar}^+ + e$	$K_{iz}$	$6.2 \times 10^{-16}$

For low-pressure gas, Doppler broadening is more dominant than pressure broadening because the Doppler linewidth is much larger than the Lorentz linewidth, and the trapping factor of the Doppler line shape is much smaller than that of Lorentz line shape. At high pressure, pressure broadening is more dominant than Doppler broadening.

From Paschen's breakdown theory, it is well known that no breakdown happens for  $pd < 0.1 \text{ Torr} \cdot \text{cm}$  for a dc discharge of Ar gas, where  $p$  is the gas pressure and  $d$  is the gap distance. In order to sustain discharges in the low-pressure regime, an electron beam is injected from the cathode with a current density of  $0.1 \text{ mA}/\text{cm}^2$  and a thermal energy of 0.5 eV (case 1). We are especially concerned with the temperature-limited mode of a beam-driven discharge,<sup>14</sup> in which electron beams are accelerated in the cathode sheath to have enough energy to ionize neutral gas in the bulk region. In addition, the radial losses of electrons and ions by ambipolar diffusion and recombination at the wall is also assumed in this case.<sup>15</sup>

In the high-pressure regime (case 2), the breakdown is triggered by the secondary electron emission by ion impact collisions on the cathode instead of the injected electron beam.

Electron impact collisions such as ionization, excitation, elastic scattering, and ion impact collisions such as charge exchange and scattering are simulated by the PIC-MCC method. The model also includes the step ionization from the electron impact collision with excited-state atoms. Other collisions are treated with a fluid model. Atomic collisions between neutral species include collisional quenching from the metastable to the radiative states, quenching from the excited states to the ground state, and the ionization by the collisions between excited states. The rate coefficients are listed in Table II.

## III. SIMULATION RESULTS

### A. Low-pressure discharge

The simulation results for the Doppler broadening case (case 1) are shown in Fig. 1. At  $t=70 \mu\text{s}$ , the metastable state is almost saturated, because of the large diffusion loss. At this time, the diffusion loss rate is almost similar to the production rate. Because of the large diffusion loss and the smaller excitation rate than the ionization rate, the densities of the excited states saturate earlier than those of electrons and ions. The resonant quenching rate is about 0.3% of the production rate, and the collisional quenching rate is less than 0.02%, thus negligible. The step ionization from the excited states is also negligible because of low metastable density compared with ground-state density.

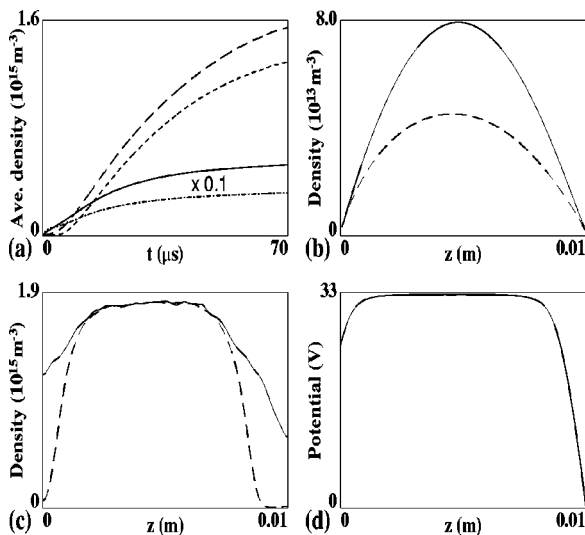


FIG. 1. Simulation results of case 1 with the cathode at  $z=0.01$  m. (a) Time evolution of spatially averaged densities of electrons (dotted) and ions (dashed), radiative (chain) and metastable (solid) excited states. The densities of excited states are exaggerated by factor of 10. (b) Density profiles of metastable (solid) and radiative (dashed) excited states, (c) density profiles of electrons (dashed) and ions (solid), and (d) time average potential profile. The profiles are obtained at  $t=70 \mu s$ .

**B. High-pressure discharge**

The simulation results for the Lorentz broadening case (case 2) are shown in Fig. 2. In this case, the decay time of the radiative state increases more than a few thousand times because of the large absorption coefficient. As shown in Fig. 2(a), the metastable density almost saturates by  $10 \mu s$  because the loss rate by resonant quenching is high, while the diffusion loss rate is not dominant in this case, about 2.6% of the production rate. The collisional quenching rate is also small, about 0.54%. The electron impact ionization from the

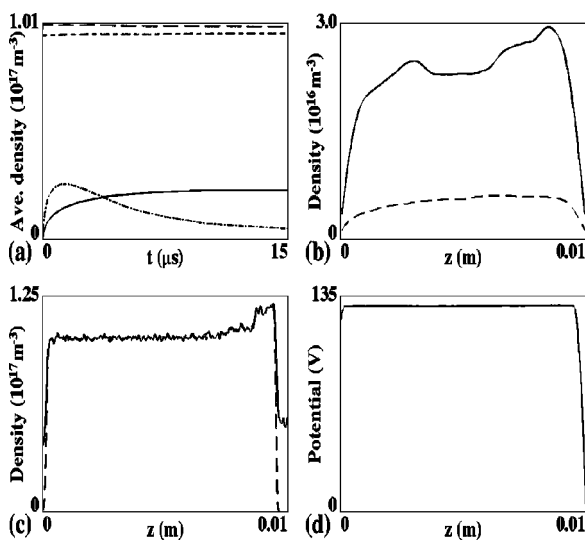


FIG. 2. Simulation results of case 2 with the cathode at  $z=0.01$  m. (a) Time evolution of spatially averaged densities of electrons (dotted) and ions (dashed), radiative (chain) and metastable (solid) excited states. (b) Density profiles of metastable (solid) and radiative (dashed) excited states, (c) density profiles of electrons (dashed) and ions (solid), and (d) time average potential profile. The profiles are obtained at  $t=15 \mu s$ .

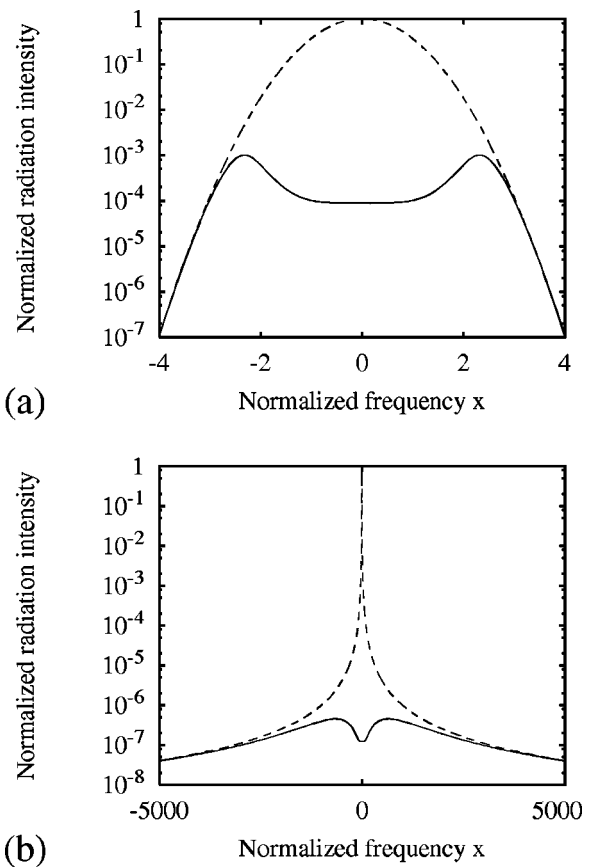


FIG. 3. Normalized spectral radiation flux profiles at the cathode (solid) and those of nonabsorbed line shapes (dashed) for (a) case 1 and (b) case 2, where  $x$  is a normalized frequency which is defined as  $x=2(\nu-\nu_0)/\Delta\nu^L$  and  $x=2\sqrt{\ln 2}(\nu-\nu_0)/\Delta\nu^D$  for Lorentz and Doppler line shapes, respectively. Here,  $\Delta\nu^D=5.59$  GHz for case 1 and  $\Delta\nu^L=0.12$  GHz for case 2.

excited states is about 8.4% of that from the ground state. As we increase gas pressure, this ratio increases; therefore, the simulation of the metastable state is important for the evolution of the steady state. The important role of step ionization of the metastable atoms in argon glow discharges was reported for simulations using fluid models.<sup>5,16</sup>

**C. Radiation emission**

Figure 3 shows the normalized spectra of the emitted radiation intensity at the cathode. Because of high-absorption rate near the line center, emission from the wings is dominant. The intensity ratios of ideal emission (without absorption, dashed line) to the real emission (solid line) are 0.11% for case 1 and 0.058% for case 2, which have the same order of magnitude as the inverses of trapping factors of the lowest modes, 0.13% and 0.061% for each case.

The ohmic heating and radiation loss powers are listed in Table III for each case. The radiation power loss is 1.51% of the electron ohmic heating for case 1, and 2.53% for case 2; therefore, it is observed that the radiation power loss in Ar glow discharges is very small compared with the power delivered to electrons by ohmic heating in the simulated parameter regimes. Thus, photons do not play an important role in the energy transfer. The ratio increases as the electron energy loss due to the excitation collision increases. Also, for highly

TABLE III. Power balance of dc Ar discharges. Here,  $L$  is the system length which is 0.01 m in these cases,  $\mathbf{J}_e$  and  $\mathbf{J}_i$  are electron and ion current densities, and  $\mathbf{E}$  is the electric field.

Power loss (W/m <sup>2</sup> )	Case 1	Case 2
Electron ohmic heating $\int_0^L \mathbf{J}_e \cdot \mathbf{E} dz$	24.91	947.62
Ion ohmic heating $\int_0^L \mathbf{J}_i \cdot \mathbf{E} dz$	3.35	38150
Radiation flux at the cathode	0.153	12.6
Radiation flux at the anode	0.223	11.4
(Radiation loss)/(electron ohmic heating)	1.51%	2.53%

collisional system, the ratio increases for short discharge length because the radiation loss increases for the low-opacity  $k_0 L$ , where  $k_0$  is the absorption coefficient at the line center and  $L$  is the system length.

#### D. Effects of nonuniform ground-state density

In order to investigate the effect of the nonuniform ground-state density on pressure broadening, we simulate the change of the neutral gas density profile for case 2. We assume three parabolic neutral gas density profiles for which total pressures in the system are homogeneous. Figure 4 shows the gas density profiles, the density distributions of the metastable and radiative excited states, and the radiation flux spectra at the anode wall, at  $z=0$ . As the pressure near the boundary increases, the densities of both the radiative and the metastable states increase there. The density profile of the radiative state does not have big humps near the boundary, unlike the metastable profile, due to redistribution by radiation transport.

Even though the radiative state density increases near the wall for the high-gas density gradient case, the spectral ra-

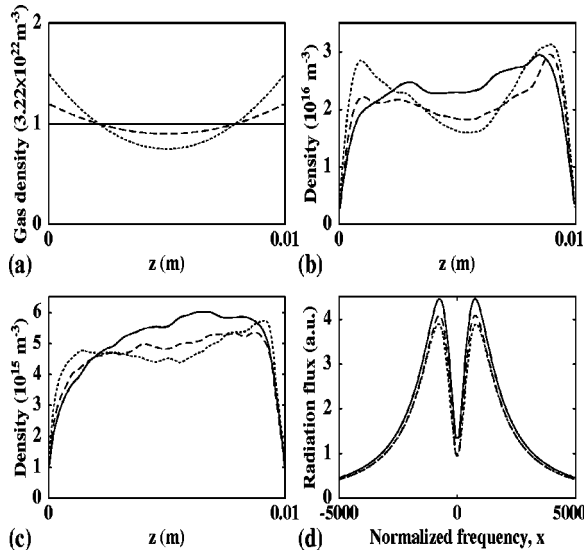


FIG. 4. The variation of the neutral gas density profile for case 2. (a) Neutral gas density profiles normalized to the density of 300 K, 1 Torr Ar gas,  $n_0 = 3.22 \times 10^{22} \text{ m}^{-3}$ . The ratios of the minimum to the maximum gas densities are 1 (solid), 0.75 (dashed), and 0.5 (dotted), respectively. (b) Metastable state density profiles, (c) radiative state density profiles, and (d) spectral radiation flux profiles at the anode,  $z=0$  m. The normalized frequency  $x$  is  $2(\nu - \nu_0)/\Delta\nu_0^L$ , and  $\Delta\nu_0^L$  is calculated from Eq. (12) of Part I with the density  $n_0$ .

diation flux decreases as the neutral gas density increases near the boundary because the reabsorption rate of photons also increases near the wall.

#### IV. COMPARISON WITH HOLSTEIN'S SOLUTION

The radiation transport equation of radiative excited state is

$$\frac{\partial n^r(\mathbf{r}, t)}{\partial t} = E(\mathbf{r}, t) - \frac{1}{\tau_v} n^r(\mathbf{r}, t) + \frac{1}{\tau_v} \int n^r(\mathbf{r}', t) G(\mathbf{r}, \mathbf{r}') d\mathbf{r}', \quad (1)$$

where  $n^r(\mathbf{r}, t)$  is the density of the radiative excited state,  $G(\mathbf{r}, \mathbf{r}')$  is the kernel (or propagator) function of the radiative state, and  $E(\mathbf{r}, t)$  is the effective production rate. The second and the third terms on the right-hand side (rhs) represent the self-decay of the resonant state and the reabsorption of photons emitted from other positions, respectively.  $E(\mathbf{r}, t)$  is defined as

$$E(\mathbf{r}, t) \equiv P_r(\mathbf{r}, t) + \nabla \cdot D_r \nabla n^r(\mathbf{r}, t) + K_r n_e(\mathbf{r}, t) n^m(\mathbf{r}, t) - [K_{cq} n_g(\mathbf{r}, t) + 2K_{iz} n^*(\mathbf{r}, t)] n^r(\mathbf{r}, t) - P_{r \rightarrow iz}(\mathbf{r}, t), \quad (2)$$

where  $P_r$  and  $P_{r \rightarrow iz}$  are the production rate of the radiative excited state by electron-neutral collisions and the loss rate of the radiative state by step ionization by electron collision.  $D_r$  is the diffusion coefficient,  $n^m(\mathbf{r}, t)$  is the density of the metastable state, and  $n^*(\mathbf{r}, t)$  is the summation of  $n^m(\mathbf{r}, t)$  and  $n^r(\mathbf{r}, t)$ .  $K_r$ ,  $K_{cq}$ , and  $K_{iz}$  are the rate coefficients for quenching and atomic ionization as listed in Table II.

If we neglect  $E(\mathbf{r}, t)$  in Eq. (1), it is exactly the same as the Holstein equation, for which the general solution is

$$n^r(\mathbf{r}) = \sum_j \alpha_j \psi_j(\mathbf{r}) \exp\left(-\frac{t}{g_j \tau_v}\right), \quad (3)$$

where  $\psi_j(\mathbf{r})$  is the eigenfunction,  $\alpha_j$  is the expansion coefficient, and  $g_j$  is the trapping factor of the  $j$ th mode. For planar geometry, the eigenfunction can be approximated by sinusoidal functions.<sup>13</sup> For even modes  $m=2j$  ( $j=0, 1, 2, \dots$ ),

$$\psi_m(z) = \sqrt{\frac{2}{L}} \left[ 1 + \frac{\sin(\lambda_m \pi)}{\lambda_m \pi} \right]^{-1/2} \cos\left[ \frac{\lambda_m \pi}{L} \left( z - \frac{L}{2} \right) \right], \quad (4)$$

and for odd modes  $m=2j+1$  ( $j=0, 1, 2, \dots$ ),

$$\psi_m(z) = \sqrt{\frac{2}{L}} \left[ 1 - \frac{\sin(\lambda_m \pi)}{\lambda_m \pi} \right]^{-1/2} \sin\left[ \frac{\lambda_m \pi}{L} \left( z - \frac{L}{2} \right) \right], \quad (5)$$

and  $g_j$  and  $\lambda_j$  can be calculated as shown in Molisch *et al.*<sup>13</sup>

In this model, we consider the effective production rate  $E(\mathbf{r}, t)$  also as defined in Eq. (2) so that the steady state equation becomes

$$E(\mathbf{r}) = \frac{1}{\tau_v} n^r(\mathbf{r}) - \frac{1}{\tau_v} \int n^r(\mathbf{r}') G(\mathbf{r}, \mathbf{r}') d\mathbf{r}'. \quad (6)$$

If we expand the steady-state quantities with the eigenfunctions of Holstein's solution

$$n^r(z) = \sum_j \alpha_j \psi_j(z), \tag{7}$$

$$E(z) = \sum_j \beta_j \psi_j(z), \tag{8}$$

and

$$\int \psi_j(\mathbf{r}') G(\mathbf{r}, \mathbf{r}') d\mathbf{r}' = \left(1 - \frac{1}{g_j}\right) \psi_j(z). \tag{9}$$

Therefore, Eq. (6) can be represented as

$$\alpha_j = \tau_v g_j \beta_j, \tag{10}$$

for the  $j$ th mode. With this relation, we can compare the radiation trapping result of the radiation transport coupled particle-in-cell (RT-PIC) model with Holstein's eigenmode solution. Equation (10) is valid only for the steady state. In order to determine the steady state, we introduce the relative change of the radiative state density at the  $k$ th cell

$$\begin{aligned} \delta_k(t) &= \frac{n_k^{(t)} - n_k^{(t-\Delta t)}}{n_k^{(t)}} \\ &= \frac{\Delta t}{n_k^{(t)}} \left[ E_k^{(t-\Delta t/2)} + \frac{1}{\tau_v} \left( \sum_{m=1}^{N_c} A_{km} n_m^{(t-\Delta t/2)} - n_k^{(t-\Delta t/2)} \right) \right], \end{aligned} \tag{11}$$

and the summation over total number of cells  $N_c$

$$\delta(t) = \frac{1}{N_c} \sum_{k=1}^{N_c} \delta_k(t), \tag{12}$$

which goes to zero at steady state.

The comparisons of simulation results at steady state with Holstein's solution are shown in Figs. 5 and 6. The relative change of radiative state density  $\delta$  is  $3.4 \times 10^{-7}$  for case 1 at  $70 \mu s$  and  $1.0 \times 10^{-7}$  for case 2 at  $15 \mu s$ . Figures 5(a) and 6(a) show the densities of the radiative excited state of each case compared with the lowest eigenmode and the summation of the first 20 modes of Holstein's eigenfunction. For both of the cases, the eigenmodes represent the density profiles very well, and the lowest mode is dominant. Figures 5(b) and 6(b) show the effective production rate profiles of each case compared with the lowest eigenmode and the summation of the first 20 modes of Holstein's eigenfunction. The eigenmode description is adequate for the effective production rate profiles, too. Figures 5(c) and 6(c) compare the left-hand side (lhs) and the rhs terms of Eq. (10), and Figs. 5(d) and 6(d) shows the relative errors of each mode which is defined as

$$\varepsilon_j = (\tau_v g_j \beta_j - \alpha_j) / \alpha_0, \tag{13}$$

for the  $j$ th mode. The relative error of the lowest mode for the Doppler line shape (case 1) is 0.11%, and that for the Lorentz line shape (case 2) is 1.83%, which are within the allowable error limit. These small errors exceed the explicit

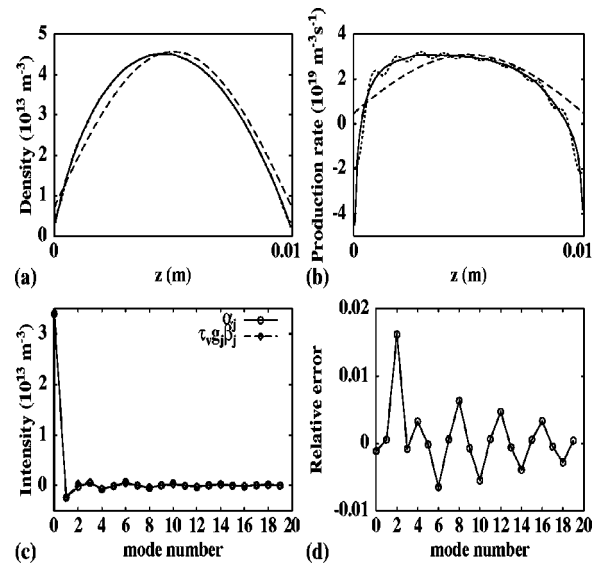


FIG. 5. Comparison results of case 1 at  $70 \mu s$  with a fitting equation from Ref. 13 for the solution of the Holstein equation. (a) Density profiles of radiative excited state (solid) and the lowest mode of Holstein's solution (dashed), and the summation of the first 20 modes (dotted). (b) Effective production rate (solid) and the lowest mode representation for it (dashed), and the summation of the first 20 modes (dotted). (c) Expansion coefficient for each mode and corresponding quantity with effective production rate by Eq. (10), and (d) relative error calculated with Eq. (13).

error limit from the measurement of steady state and from the approximation of the eigenmode and trapping factor.

In Fig. 7, we compared the results of the full radiation transport simulation with the results obtained without radiation transport, and with a simplified radiation transport

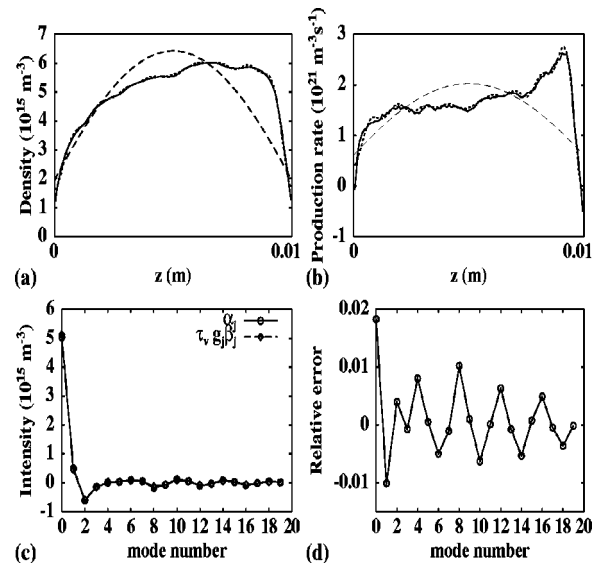


FIG. 6. Comparison results of case 2 at  $15 \mu s$  with a fitting equation from Ref. 13 for the solution of the Holstein equation. (a) Density profiles of radiative excited state (solid) and the lowest mode of Holstein's solution (dashed), and the summation of the first 20 modes (dotted). (b) Effective production rate (solid) and the lowest mode representation for it (dashed), and the summation of the first 20 modes (dotted). (c) Expansion coefficient for each mode and corresponding quantity with effective production rate by Eq. (10), and (d) relative error calculated with Eq. (13).

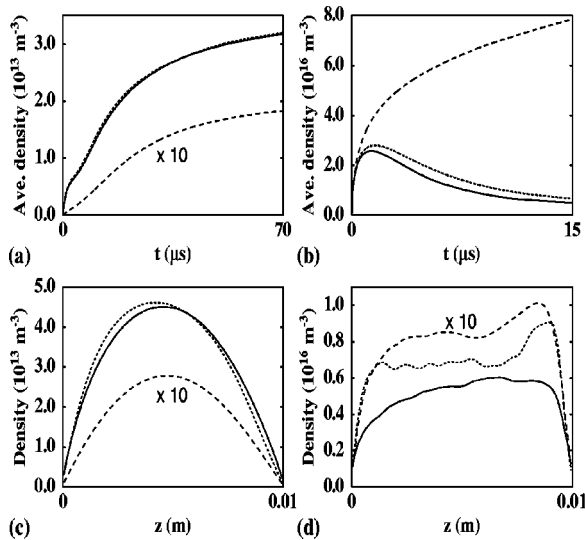


FIG. 7. Time evolutions of the radiative excited-state density for full radiation transport simulation (solid) from Eq. (1), for a trapping factor correction in decay rate (dotted) from Eq. (15), and without radiation transport (dashed) from Eq. (14), for (a) case 1 and (b) case 2. Density distribution of the radiative excited state for (a) case 1 at 15  $\mu\text{s}$ , and (b) case 2 at 70  $\mu\text{s}$ . In (a), (c), and (d), the dashed lines are reduced by factor of 10.

model with an effective decay rate  $1/g_0\tau_v$ . Each case is equivalent to the replacement for Eq. (1) with

$$\frac{\partial n^r(\mathbf{r}, t)}{\partial t} = E(\mathbf{r}, t), \quad (14)$$

or

$$\frac{\partial n^r(\mathbf{r}, t)}{\partial t} = E(\mathbf{r}, t) - \frac{1}{g_0\tau_v} n^r(\mathbf{r}, t). \quad (15)$$

For the low-pressure case, the lowest mode is very close to the exact solution as shown in Figs. 5(a) and 5(b). Thus, the approximation using the effective decay rate  $1/g_0\tau_v$  produces almost the same results as the full simulation due to small radiation trapping. For the high-pressure case, however, the discrepancy between the lowest mode and the exact solution is not negligible as shown in Figs. 6(a) and 6(b). Therefore, the approximate result shows significant difference. There are many models using this approximation for lamp discharges or laser induced plasmas, but they are not appropriate if the density distribution of the radiative state has a big difference from the lowest mode profile of Holstein's solution. The discrepancy becomes severe for the nonuniform ground-state density profile as shown in Fig. 4(c).

As shown in the dashed line of Fig. 7, the results with Eq. (14) show a large discrepancy with the exact solution. If we do not consider the metastable and radiative states separately in the excitation cross section, the obtained excited-state density is described by Eq. (14), which overestimates the excited-state density. Many plasma models treat the excited state in this way, and therefore, are not adequate for the simulation of lighting devices.

## V. SUMMARY AND DISCUSSIONS

We present simulation results of the radiation transport coupled particle-in-cell simulation for the one-dimensional planar model. This model is applied to simulate Ar glow discharges in two pressure regimes where Doppler and pressure broadenings are dominant, respectively. The radiation flux spectra are calculated from the radiative state distribution, and the total radiation power losses are compared with the ohmic heating of plasmas. The ratio of radiation power to the electron ohmic heating is below 3% for the parameter regime of our simulation.

The simulation results are compared with the eigenmode solution of the Holstein equation for the steady state,<sup>13</sup> and they agree well with each other within 2% of error.

For the low-pressure case, the lowest eigenmode represents the exact profiles of the radiative state and the effective production rate very well. Therefore, the approximation using the effective decay rate of  $1/g_0\tau_v$  is valid. For the high-pressure regime, the deviation between the lowest eigenmode and the exact solution is not negligible, and a full radiation transport simulation is necessary. The deviation increases for nonuniform ground-state distributions which have higher density near the boundary than at the center.

The numerical calculation of the radiation transport model is expensive only for the calculation of the matrix elements  $A_{km}$ , which is the probability for a photon emitted from the  $m$ th cell to be reabsorbed in the  $k$ th cell. The CPU time needed to evolve the excited states is very small compared with that needed to move plasma particles in the PIC-MCC model, because the former depends on the number of cells for the radiation transport simulation and the latter depends on the number of simulated particles. For sufficient statistics, we use more than  $10^4$  super particles, each of which represents a large number of real particles ( $10^5 - 10^8$ ).

When we consider a static ground-state density, we calculate the matrix elements  $A_{km}$  only once at the beginning of the simulation; thus the radiation transport calculation does not affect the simulation speed. However, when we consider a time-varying ground-state density for a more self-consistent model, we should recalculate the  $A_{km}$  elements for every neutral gas evolution time step,  $\Delta t_g$ , thus affects the simulation speed.

When we simulate case 2 given in Table I using a Pentium PC with a 400 MHz processor, it takes about four days to reach 15  $\mu\text{s}$ . In this case, the CPU time needed for the radiation transport part is less than 5% of that for the PIC-MCC part.

## ACKNOWLEDGMENTS

We are grateful to Dr. Darryl Michael and Dr. John Ingold for many discussions about fluorescent lamp discharges. We also appreciate the helpful discussion with Dr. Greg Parker about radiation transport and the consultation with Professor C. K. Birdsall.

This work was supported in part by General Electric Company Contract No. GE-20000181.

- <sup>1</sup>J. H. Ingold, "Radiative process in discharge plasmas," in *Radiative Processes in Discharge Plasmas*, edited by J. M. Proud and L. H. Luessen (NATO ASI Series, New York, 1985), Vol. 149, pp. 27–37.
- <sup>2</sup>T. Holstein, *Phys. Rev.* **72**, 1213 (1947).
- <sup>3</sup>T. Holstein, *Phys. Rev.* **83**, 1159 (1951).
- <sup>4</sup>L. M. Biberman, *Zh. Eksp. Teor. Fiz.* **17**, 416 (1947).
- <sup>5</sup>C. M. Ferreira, J. Loureiro, and A. Ricard, *J. Appl. Phys.* **57**, 82 (1985).
- <sup>6</sup>J. B. Anderson, J. Maya, M. W. Grossman, R. Lagushenko, and J. F. Waymouth, *Phys. Rev. A* **31**, 2968 (1985).
- <sup>7</sup>A. F. Molisch, B. P. Oehry, W. Schupita, and G. Magerl, *Comput. Phys. Commun.* **93**, 127 (1993).
- <sup>8</sup>J. E. Lawler, G. J. Parker, and W. N. G. Hitchon, *J. Quant. Spectrosc. Radiat. Transf.* **49**, 627 (1993).
- <sup>9</sup>J. P. Verboncoeur, M. V. Alves, V. Vahedi, and C. K. Birdsall, *J. Comput. Phys.* **104**, 321 (1993).
- <sup>10</sup>A. C. G. Mitchell and M. W. Zemansky, *Resonance Radiation and Excited Atoms* (Cambridge University Press, New York, 1961).
- <sup>11</sup>M. G. Payne, J. E. Talmage, G. S. Hurst, and E. B. Wagner, *Phys. Rev. A* **9**, 1050 (1974).
- <sup>12</sup>H. A. Post, *Phys. Rev. A* **33**, 2003 (1986).
- <sup>13</sup>A. F. Molisch, B. P. Oehry, W. Schupita, and G. Magerl, *J. Quant. Spectrosc. Radiat. Transf.* **48**, 377 (1992).
- <sup>14</sup>H. J. Lee and J. K. Lee, *Phys. Plasmas* **5**, 2878 (1998).
- <sup>15</sup>M. A. Lieberman and A. J. Lichtenberg, *Principles of Plasma Discharges and Materials Processing* (Wiley, New York, 1994), Chaps. 5 and 10.
- <sup>16</sup>D. P. Lymberopoulos and D. J. Economou, *J. Appl. Phys.* **73**, 3668 (1993).